APPLIED SCIENCES AND ENGINEERING

Leaf-inspired homeostatic cellulose biosensors

Ji-Yong Kim[1,2†], Yong Ju Yun[3†], Joshua Jeong[2], C.-Yoon Kim[4], Klaus-Robert Müller[5,6,7], Seong-Whan Lee[1,5*]

An incompatibility between skin homeostasis and existing biosensor interfaces inhibits long-term electrophysiological signal measurement. Inspired by the leaf homeostasis system, we developed the first homeostatic cellulose biosensor with functions of protection, sensation, self-regulation, and biosafety. Moreover, we find that a mesoporous cellulose membrane transforms into homeostatic material with properties that include high ion conductivity, excellent flexibility and stability, appropriate adhesion force, and self-healing effects when swollen in a saline solution. The proposed biosensor is found to maintain a stable skin-sensor interface through homeostasis even when challenged by various stresses, such as a dynamic environment, severe detachment, dense hair, sweat, and long-term measurement. Last, we demonstrate the high usability of our homeostatic biosensor for continuous and stable measurement of electrophysiological signals and give a showcase application in the field of brain-computer interfacing where the biosensors and machine learning together help to control real-time applications beyond the laboratory at unprecedented versatility.

INTRODUCTION

Continuous monitoring of human physiological signals on the skin is critical in diverse fields ranging from medical aspects such as disease diagnosis, rehabilitation, and recovery to neurotechnology, gaming, and entertainment (*1*–*6*). Existing noninvasive electrophysiological (EP) biosensors (*7*–*12*) have shown impressive performances, but they do not consider skin homeostasis (*1*, *13*, *14*). Furthermore, long-term biosafety has not been verified dermatologically (*1*, *15*, *16*).

The skin (*15*, *16*) is vital for aspects of homeostasis (*14*) that include protection, regulation of body temperature, water balance, absorption of materials, and others. Accurate measurement of EP signals on the skin can be increased by an in-depth understanding of the complex structure and function of the skin (*1*, *13*).

To pursue this goal, the botanical leaf is adopted as a useful reference. A leaf system consists of three main tissues: epidermis, mesophyll, and vascular tissue. The epidermis contains cuticle (*17*) and stomata (*18*). Leaf homeostasis maintains the water content inside the plant by regulating stomata against abiotic stresses such as flooding and drought (*18*–*21*). We will, in the following, exploit and mimic these properties of leaves to construct a homeostatic biointerface that is compatible with the human skin.

To develop homeostatic materials, which are the core component of the homeostasis system, a few studies proposed complex synthesis techniques (*22*, *23*). However, we explore hints for the most natural homeostatic material within the leaf system.

Cellulose is the main component of the cell wall of a leaf (*24*–*26*). The presence of cellulose enables cells to reversibly swell as a result of water absorption (*27*, *28*). Thus, wet cellulose exhibits a unique combination of excellent flexibility, self-healing capability, and outstanding biocompatibility.

We have therefore analyzed properties that change in mesoporous cellulose membranes (CMs) (*29*, *30*) during the absorption of saline solution, which is harmless to the skin. This analysis revealed that the CM markedly transforms its properties to become a homeostatic material of self-regulation at approximately 85% of the swelling (*27*, *28*) process. In addition, we verified the long-term biosafety of CM based on in-depth dermatological tests.The performance of cellulose biosensors (CSs) is shown to compare well to that of conductive gel sensors (GSs) (*7*, *8*) that can establish a reliable conductive interface on the skin in the presence or absence of hair layers.

In our endeavor to imitate the architecture of the leaf system, the biosensor components include a surface designed to absorb, store, and diffuse water; a supporting structure to protect and support the surface from the outside; and a gate structure regulated by pressure (Fig. 1A).The key mechanism to construct a homeostatic interface between the skin and sensor surface is shown in Fig. 1B. In this mechanism, ions and water molecules inside the mesopores of the swollen CM spontaneously permeate into the inner layers of skin through the pores of the stratum corneum by diffusion gradient, thereby noninvasively increasing the contact surface area with the skin (fig. S1, A to E). When changes such as sweat secretion occur in the skin, the sweat penetrates into the CM pores by diffusion, keeping a stable conductive path between the skin surface and CM (fig. S1, A to C).

The high performance of CS on various locations of human skin could be verified by measuring representative EP signals [here electroencephalogram (EEG), electrooculogram (EOG), electromyography (EMG), and electrocardiogram (ECG); Fig. 1B, ii] (*2*), and the CS stability and robust quality are demonstrated below for a direct, real-time control application using machine learning (*31*, *32*) (Fig. 1B, iii).

RESULTS

Figure 1C presents a schematic illustration of the CS. The structure consists of a reservoir for saline solution, an Ag/AgCl electrode, a glass fiber membrane (GM) that supports and preserves the CM, and the CM with a perforated pore. Figure S2 (A and B) shows the surface detail and cross-sectional morphology of both the CM and GM.

[1]Department of Brain and Cognitive Engineering, Korea University, Seoul, Republic of Korea. [2]NeuroPitta Inc., Seoul, Republic of Korea. [3]Graduate School of Energy and Environment (KU-KIST Green School), Korea University, Seoul, Republic of Korea. [4]Department of Medicine, Konkuk University, Seoul, Republic of Korea. [5]Department of Artificial Intelligence, Korea University, Seoul, Republic of Korea. [6]ML Group and BIFOLD, Berlin Institute of Technology, Berlin, Germany. [7]Max Planck Institute for Informatics, Saarbrücken, Germany.
*Corresponding author. Email: sw.lee@korea.ac.kr
†These authors contributed equally to this work.

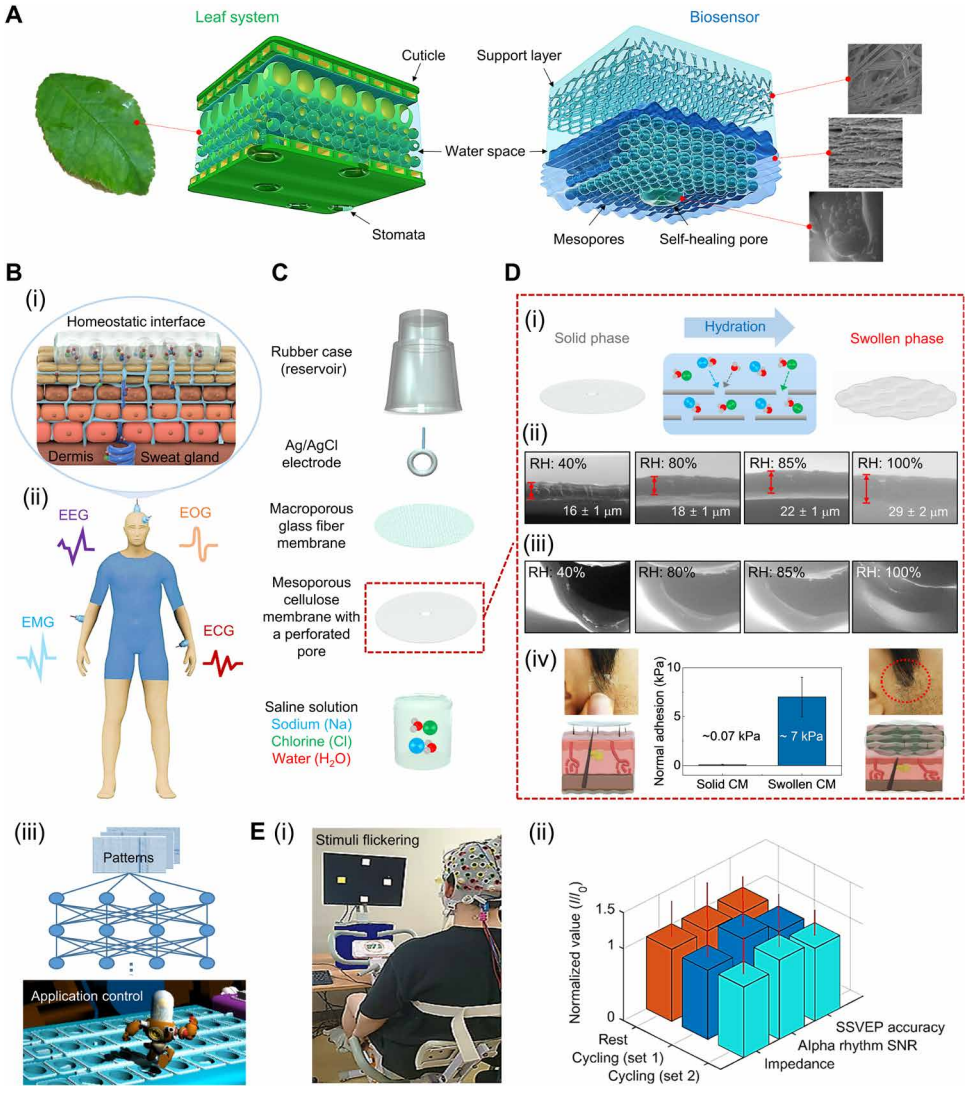

Fig. 1. Design, mechanism, and applications of cellulose-based biosensor. (**A**) Structure of the proposed biosensor surface based on two types of porous membranes that mimic the leaf architecture. (**B**) (i) Illustration of a homeostatic interface between skin and sensor surface. (ii) Schematic illustration of measurement locations on a human model for multiple acquisition of EP signals. (iii) The flow of application control through artificial intelligence learning. (**C**) Exploded-view schematic illustration of a cellulose biosensor (CS). (**D**) (i) Schematic illustration showing the direction of ion/water permeation along the cellulose porous layers (center). (ii and iii) ESEM images of the cross section of CMs under different conditions of RH. In (iii), the perforated pore was closed by the self-healing effect of CM. (iv) Comparison of the adhesion strengths of solid and swollen CM. (**E**) (i) Photograph of an individual performing the steady-state visual evoked potentials paradigm while pedaling an exercise bike. (ii) Normalized comparison of the performances of CSs in resting, cycling set 1, and cycling set 2, respectively. Photo credit: Ji-Yong Kim, Korea University.

To reveal the underlying mechanism of the observed CM swelling, comprehensive analyses are performed. These include the change of surface morphology and thickness as a function of relative humidity (RH) using environmental scanning electron microscopy (ESEM) (*33*, *34*), the change of dry/wet adhesion strength in an adhesion test, and the variation of ionic conductivity under a function of RH (*35*).

Immersion of a CM in saline solution leads to infiltration of two types of hydrated ions and water molecules between cellulose nano- and microfibril sheets (Fig. 1D, i). Cellulose is an organic polymer whose chains are linked via hydrogen bonding, and water or ion molecules participate in the binding sites, causing the polymer volume to increase. This results in swelling. The saline solution permeates inside the CM by changes in the contact angle according to drop volume (fig. S2C, i and ii). The diffusion rate at which CM diffuses the electrolyte is about 0.41 ± 0.05 μl/min.

We determined the changes of thickness of the CM in an ESEM chamber, where the RH around the dry specimen has increased from 40 to 100%. As shown in the ESEM images of the CM (Fig. 1D, ii), the CM underwent a drastic thickness change as the environmental humidity reached approximately 85% by absorbing water molecules. The more detailed ESEM imaging results are shown in fig. S2D.

Wet adhesion (7.18 ± 1.79 kPa) of the CM on hairy skin is observed to increase by nearly 100-fold (Fig. 1D, iv, and fig. S1, F and G). The swollen CM displays pronounced adhesive capability under wet conditions on hairy skin without leaving a trace after detachment through an effortless peel-off procedure.

Morphology changes of the perforated pore inside the CM show little change in the pores until an RH of approximately 80% (fig. S3, A and B). At RHs ≥85%, the self-healing effect of CM on the pore becomes evident (Fig. 1D, iii), and at 100% RH, the pore is mostly closed. This pore reopens or recloses because of the external (contact pressure) or internal pressure (swelling)—a concept similar to the leaf stoma (*18*). Using this property of the CM, a controllable releasing mechanism is devised based on the self-healing gate capable of discharging a small amount of electrolyte by contact pressure (fig. S3, D and E).

At an RH of 40%, the CM is nonconductive (*36*) with an electrical resistance of 10^9 ohm·cm (Fig. 2A). At RHs between 60% and 80%, the electrical resistance slowly decreases to 1.0×10^5 ohm·cm in a stepwise manner (*35*). At an RH of approximately 85%, the CM thickness markedly expands to 22 ± 1 μm and resistance significantly decreases to 5.2×10^4 ohm·cm (Figs. 1D, ii, and 2A). This electrical resistance level, which is lower by roughly four orders of magnitude (1.9×10^4 times) compared to the initial value, is conveniently the same level as that of a conductive gel (CG). At RHs ≥85%, the resistance reaches saturation level (Fig. 2A).

Long-term conductivity and electromechanical stability under bending deformations are critical requirements for applications in skin electronics (*11*, *12*). When investigating the ionic conductivity of the CM (swollen for 8 hours), the CM exhibits considerably improved electrical properties (Fig. 2, A and B). In particular, the conductivity value of approximately 9.23×10^{-5} S/cm was approximately four times higher than the value of CG (fig. S10) (*37*). In addition, the electrical conductivity of the CM was studied in a bending experiment: Bending by up to 1.0 mm (fig. S3G) yields no observable change in conductivity, whereas a 2.0-mm bending radius showed a decrease by approximately 2%. Long-term stability of the CM was evaluated by measuring the conductivity during 10,000 repeat bend-and-release cycles at RH >90% (fig. S3F). The conductivity remained unchanged even after 10,000 bending cycles at a bending radius of 3.0 mm (Fig. 2C). The findings provide evidence of the excellent flexibility and durability of the CM.

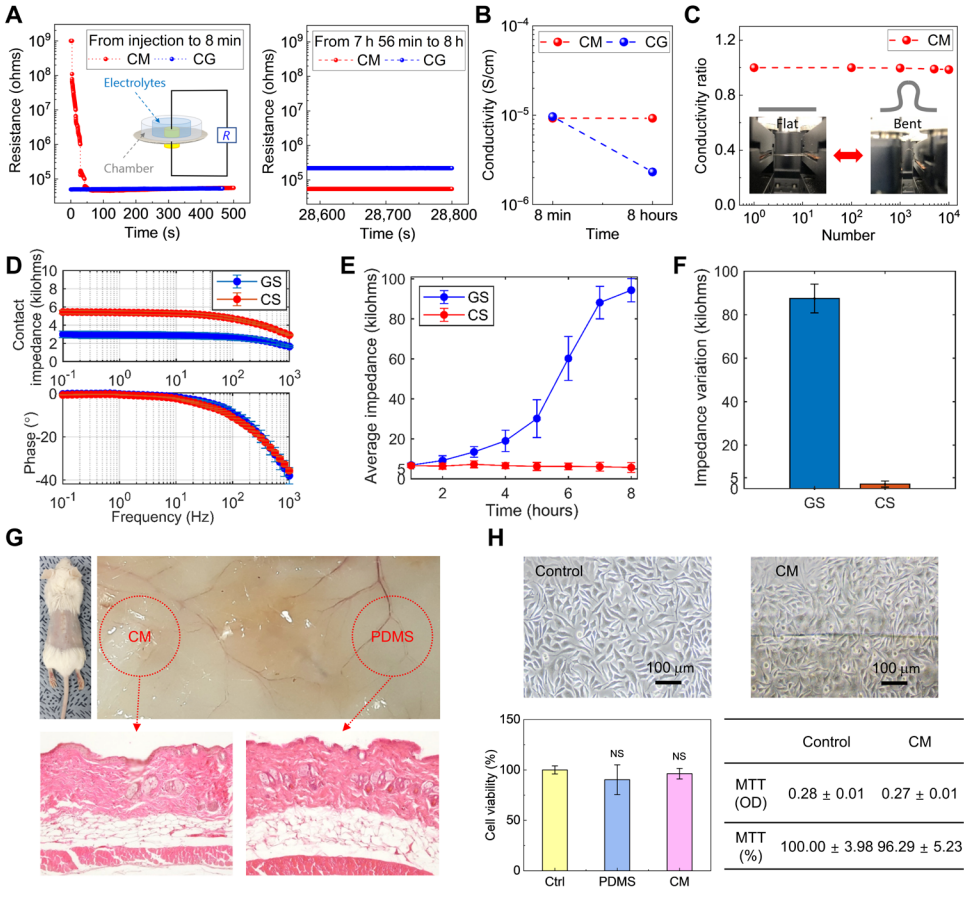

Fig. 2. Electrical characterization and biosafety test of biosensor based on CM. (**A**) Comparison of the variations of resistance values of CM and CG for 8 hours. The inset shows the resistance measurement setup. (**B**) Comparison of variations of ionic conductivity of CM and CG. (**C**) Electromechanical stability test of CMs. Data show relative variations in conductivity versus bending cycles under repeated bending to an *R* of 2.5 mm. Inset image shows the flat and bent CMs. (**D**) Electrochemical impedance spectroscopy test results of CS and GS (**E**) Comparison of time-dependent average impedance variations of CS and GS measured for 8 hours daily for 7 days. (**F**) Comparison of impedance variations during an 8-hour continuous recording daily for 7 days. (**G**) In vivo animal test of CM. The images are of a mouse implanted with a piece of CM and PDMS as a control. Images of hematoxylin and eosin (H&E)–stained tissue around the implant site of CM (left) and PDMS (right) after 14 days. (**H**) In vitro cytotoxicity test of CM. Data of human keratinocytes cell morphology and MTT assay results. CCK-8 analysis of cell proliferation on culture dish (control), PDMS, and CM during 14 days. Photo credit: Yong Ju Yun, Korea University, and C.-Yoon Kim, Konkuk University.

In vivo and in vitro biosafety test data of the CMs are essential for biosensor applications (*1*, *13*). Multiple dermatologic tests are required, including in vivo animal testing, in vitro cell culture, proliferation analysis, and skin biosafety testing. A representative image of hematoxylin and eosin (H&E)–stained tissue around the implant site of the CM could establish the absence of inflammatory responses (Fig. 2G). In vitro, most human keratinocytes on the CM were alive and spread uniformly. Furthermore, the CM showed excellent cell viability compared to the control samples (Fig. 2H and fig. S1H). These results confirm that the CM can be used for biosensors without any biosafety issues.

Electrochemical stability was also assessed. During the electrochemical impedance spectroscopy (EIS) test, contact impedances of CSs maintained an average of ≤6.0 kilohms at frequencies ranging from 10^{-1} to 10^{3} Hz (Fig. 2D). The CSs also showed a level of phase stability similar to that of GSs. Furthermore, in the open circuit potential (OCP) test of polarization voltage stability, average equilibrium potentials of Ag/AgCl and CS oscillated at a similar small magnitude (fig. S4, C and D). The findings indicate that the structures of CS have a negligible effect on the polarization voltage.

In general, the performance of biosensors is only considered reliable and robust when it generalizes across a wide range of experimental paradigms and individuals with different skin and hair types, lengths, and scalp properties (*7*). Homeostatic CSs have a homeostatic function based on the diffusion-based self-regulation and the self-healing gate–based releasing mechanism to quickly construct a conductive path on any normal skin and maintain it continuously. To demonstrate this robustness, we measure high-quality EEG at low impedances of approximately 10 kilohms (fig. S4, E to G) on both Westerners and Asians, independently of individual differences in the thickness and density of hair. Specifically, the evaluation of the CSs comprises 52 individuals with dense hair layers, including women with long hair, and overall, a highly sensitive conductive interface with a grand average impedance of 8.18 ± 5.1 kilohms is observed (table S1).

The impedance stability for long term is important because the measurement period for high-quality EP signals depends on the impedance stability (*38*). In the average results of an 8-hour continuous recording daily for 7 days, during 1-hour monitoring, both CSs and GSs provided high-quality EEG data (Fig. 3, D and E), with a very low impedance (6.64 ± 0.95 and 6.90 ± 1.06 kilohms, respectively) and a high signal-to-noise ratio (SNR) (Fig. 2E and fig. S5E). There was no significant difference in the two-sample test ($P = 0.5866$). Power spectral density (PSD) and spectrogram detected clear alpha rhythm features at approximately 10 Hz for both sensors (Fig. 3F and fig. S5, F and G).

After 8 hours, high-quality EEG measurements were still obtained with the CSs with a very low impedance (5.71 ± 2.44 kilohms) and high SNR (6.41 ± 2.58), similar to the initial value. In contrast, only low-quality EEG measurements were obtained using the GSs, with a high impedance and low SNR (Figs. 2E and 3E and fig. S5E). The difference in the two-sample test was highly significant ($P = 0.0001$).

Variation in the impedance of CSs over an 8-hour period was very small (2.09 ± 1.39 kilohms), whereas that in the impedance of GSs was excessively large (Fig. 2F). In spectrogram analysis, the CSs still displayed clear alpha rhythm patterns, which were not detected anymore with the GSs (Fig. 3F and fig. S5G). These findings confirmed that CS maintained unprecedented sensitivity with high temporal resolution of brain activities for a long time.

The effect of artifacts associated with relative motion depends on how intimate the interface between the sensor surface and skin is (*1*, *2*, *7*). We analyzed the influence of the stability of the homeostatic interface on the occurrence of severe artifacts by repeatedly detaching the sensor from the scalp (Fig. 3A and movie S2) (*39*). The initial impedance of CS was, on average, 5.78 ± 1.87 kilohms, which increased slightly to an average of 6.67 ± 1.76 kilohms after a total of 180 detachments for nine individuals (Fig. 3C). However, the impedance of GS exceeded 100 kilohms after only seven detachments, and further measurements in our system were impossible. An analysis was performed of the recovery time needed for successful remonitoring of normal EEG. When the detached sensor was reset on the skin, the average recovery time of CSs was 2.04 ± 0.65 s (Fig. 3B). A recovery time could not be determined for GSs following few detachments (fig. S7). The findings confirm the reliable stability of homeostatic CSs against severe artifacts.

Accurate measurements of EP signals of the central and peripheral nervous systems are in general use for medical diagnosis (*2*). Thus, we performed simultaneous as well as single measurements (*12*) of EP signals to demonstrate the accuracy, reliability, and broad usability of the proposed biosensor. In the single measurements, the CSs clearly captured EP signals (Fig. 3G, i) similar to those of GSs (Fig. 3G, ii, and fig. S6, A to C).

Multichannel decoding analysis of EEG and ECG measured simultaneously from the CSs in the awake state could clearly reveal the appearance of a beta wave in the EEG (*40*), and ECG-generated waveforms of approximately 0.77 s associated with cardiac systole-diastole cycle (Fig. 3, H and I) (*41*). In the drowsy state, as to be expected, alpha activity was captured in EEG (*40*), and the ECG waveforms became longer with cycles between 0.87 and 0.89 s [Fig. 3, H and I, and fig. S8; ECG cycles in the drowsy state were, on average, 0.07 ± 0.04 s longer than those in the awake state; (*41*)].

In the EEG time domain analysis of movement intention (fig. S6D), movement-related cortical potentials (*42*), which reflect cortical processes in movement planning and execution, were clearly generated approximately 1.5 s before EMG onset (Fig. 3J). The potential began to decrease negatively approximately 0.3 s after the cue sound and returned to baseline after a peak negativity at approximately 0.8 s, all in line with neurophysiological literature. These findings show exemplarily a usefulness of CSs enabling accurate simultaneous recording of EP signals across various human cognitive states.

Noninvasive brain-computer interfaces (BCIs) (*3*–*6*, *31*), which measure EEG related to brain activities using sensors placed on the scalp and process the signals using machine learning (*43*–*45*), provide a direct communication pathway between a brain and external devices. In the motor imagery (MI) paradigm (*46*, *47*) (fig. S6E), grand average event-related desynchronization/event-related synchronization (ERD/ERS) patterns (*43*, *46*, *47*) were clearly generated from C5 and C6 of the CSs (Fig. 4A). In addition, the ERD/ERS pattern changes appeared according to topographic maps of certain intervals (*45*). In case of the SSVEP (steady-state visually evoked potential) paradigm that allows the transfer of information for control by decoding frequency-locked brain states (fig. S6F) (*46*), the PSD was significantly activated at target frequencies (12, 8.57, 6.67, and 5.45) (Fig. 4B and Supplementary Text).

Monitoring faint EP signals that are easily obscured in dynamic environments that encompass various types of environmental noise, body noise, movement artifacts, and sensor misalignment is a very challenging issue (*1*, *5*, *48*). As a robustness test of our novel biosensor, we perform SSVEP paradigms while the volunteer pedals

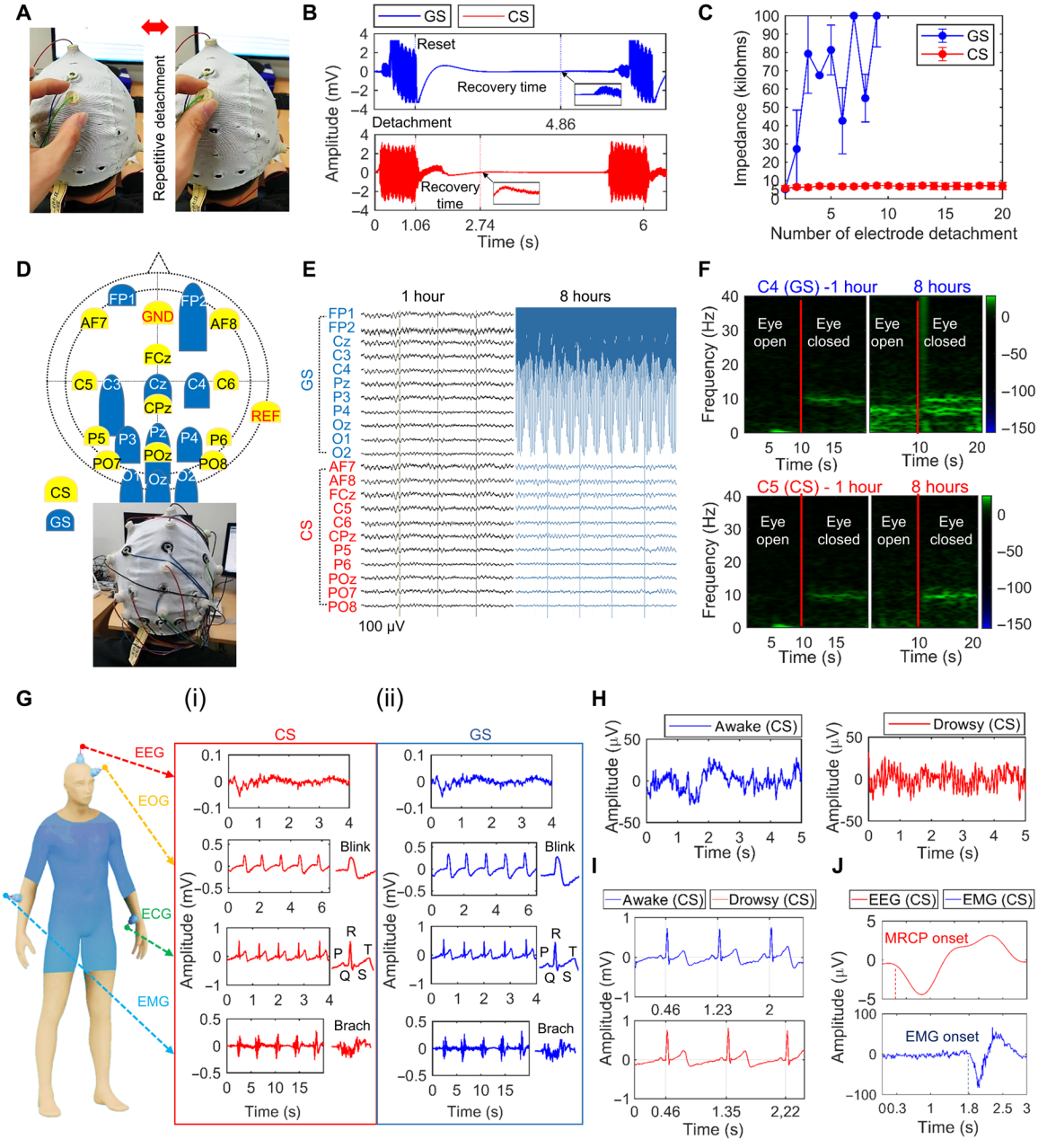

Fig. 3. Artifact-robust and long-term stable biosensors for multiple EP recording. (**A**) Photographs of CS detachment from the skin. (**B**) Recovery time of sensors for remeasurement of normal EEG when reset after detachment. (**C**) Impedance measurement according to the number of sensor detachments. (**D**) Schematic diagram and photograph of the biosensor setup for long-term EEG monitoring. (**E** and **F**) EEG raw signals and spectrograms at 1 hour and 8 hours in the eye open/closed paradigm for 8 hours. (**G**) Schematic illustration of CSs attached to the human body for recording of single EP signals. (i) EP signals of CSs. (ii) EP signals of GSs. (**H** and **I**) EEG and ECG recorded simultaneously from CSs in awake (blue) or drowsy (red) state (**J**) Time-dependent comparison of average EEG (red) and EMG (blue) recorded simultaneously from CSs when gripping a handgrip a total of 160 times across eight individuals. Photo credit: Ji-Yong Kim, Korea University.

an exercise bike (Fig. 1E and movie S1) (*49*). Without the use of artifact removal algorithms and an abrasive skin preparation gel, the CSs were able to continuously maintain low impedances and a decoding accuracy of SSVEP (Fig. 1E, ii). Furthermore, the SNR of alpha rhythms somewhat increased on the sweaty scalp (*50*). This effect occurs because the CSs have a stable equivalent circuit model against a sudden change in skin conductivity, such as that caused by sweat secretion, and the variation in CS impedance within a 4 to 8 pH range is very small (1.0 ± 1.1 kilohms) (fig. S9 and Supplementary Text) (*51*). The homeostatic interface thus has established itself as very stable and robust in dynamic environments, forming more intimate contact with the skin through sweat (fig. S1B and Supplementary Text).

Last, computer games are used as a further demonstration of BCI as they are inherently safe and attractive to a layperson (*6*). Thus, we applied the CSs to a real-time BCI avatar control game established as a benchmark for our previous real-world BCI competitions (Fig. 4C)

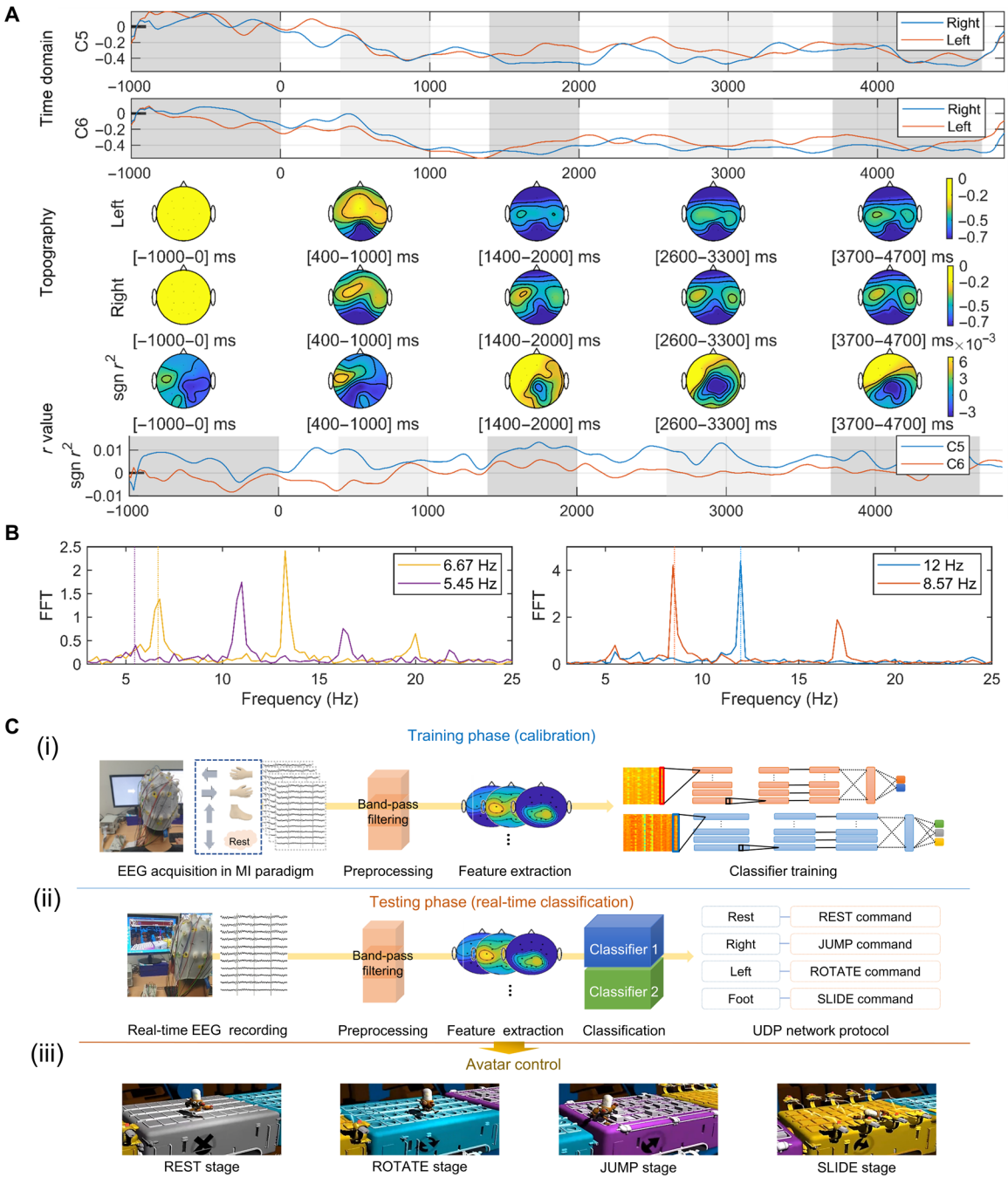

Fig. 4. Offline and real-time BCIs based on machine learning algorithms. (**A**) ERD/ERS pattern analysis of CSs in the binary MI paradigm. Grid plots of time domain for grand average EEG are shown. Topographic maps corresponding to certain intervals emphasized by gray areas in the grid plot are presented. Topographic maps and grid plot for signed *r* values (significance level) between the classes are depicted. (**B**) PSD at the POz (CS) in the SSVEP paradigm. FFT, fast Fourier transform. (**C**) Real-time BCI avatar control game system. (i) Training phase for learning classifier parameters based on deep learning in the four-class MI paradigm. (ii) Testing phase for real-time classification of motor intentions of the user. (iii) Avatar control according to stage type. Photo credit: Ji-Yong Kim, Korea University.

(*6*). Eight users successfully completed the avatar race in a reasonable average time of 177.83 ± 32.52 s using the classifiers trained by deep learning (*52*) (see Supplementary Text and movie S3). These findings establish that the CSs are able to continuously and robustly capture high temporal resolution brain patterns as a robust measurement basis for a subsequent real-time application system.

DISCUSSION

In summary, from in-depth consideration of skin homeostasis (*1*, *2*, *7*, *13*), a novel biosensor with functions such as protection, self-regulation, biosafety, and sensation required for long-time measurement was conceived. Existing EP sensors (*7*–*12*) developed with a focus on sensation or protection (table S2) are not compatible with skin homeostasis,

causing skin allergies or contact dermatitis or are being affected by sweat (*1*, *13*–*16*, *50*).

The proposed CSs that mimic the leaf homeostasis system can robustly maintain a stable skin-sensor interface by virtue of the homeostatic functionality. Specifically, the leaf-inspired convex sensor surface, which consists of two types of membrane layers, maintains conformal contact with uneven skin by the properties of adhesion, while exhibiting excellent flexibility and mechanical stability (fig. S4B). These properties are able to protect the interface stably despite physical stress such as exercise by dynamic real-world environments (Figs. 1E and 3, A to C; fig. S7; and movies S1 and S2).

The core of the homeostatic conductive interface is sustainability such as leaf homeostasis. The CSs have the self-regulation function based on continuous diffusion between the skin and the sensor surface to maintain a stable conductive interface by itself for long term (Figs. 2, E and F, and 3, E and F). Moreover, the self-healing gate–based releasing function made the CSs possible to construct a highly sensitive electrical interface even on various skins of 52 individuals with dense hair layers (fig. S4, E to G, and table S1).

CM, a nonconductive material, has never been considered for use as a main conductive component in the biosensor field (*36*). When absorbing a saline solution, CM changes to conductive homeostatic material that is compatible with the skin and can provide a reliable sensor measurement. In addition, because of the biosafety and reversible property of cellulose, CS can provide long-time usage and reusability (*27*, *28*).

In conclusion, the CSs could display very notable performance with high stability and fidelity for the total of 60 individuals. The homeostatic CSs will thus increase the repertoire of biosensor functionality for broad clinical and nonclinical applications.

MATERIALS AND METHODS

In the biosensor fabrication

The retention rate, thickness, and pressure drop of the GM (Hyundai Micro Co., Republic of Korea) were 2.7 μm, 0.53 mm, and 140 mbar, respectively. A commonly used regenerated cellulose dialysis tube with a molecular weight cutoff of 8000 to 14,000 was used as the CM. The CM had 2.5-nm-diameter pores, 50 ± 2% degree of swelling, and a thickness of 16 ± 3 μm. To mimic the water absorption and diffusion of a leaf system, a pore with a radius of around 100 μm was perforated inside the CM; this pore functioned as a gate, similar to the role of the stoma.

The CS surface was a wide ellipse, which extended the surface width as much as possible during CS swelling. To maintain the swollen phase of the CM, we constructed a reservoir of NaCl saline solution inside the CS and added Ag/AgCl to transform the ionic current to an electric current. In addition, a hydrophobic macroporous GM layer was added inside the CM to prevent direct contact between the electrical conductor and CM. The GM layer also supported the convex shape of the CM under external pressure.

Adhesion test of CM

The adhesion force of CM in the solid or swollen state was measured by 5000 *g* digital force gaze (FG-5005, Lutron, Taiwan). The average adhesion force from 10 measurements was determined.

Characterization of two types of membranes

The surface morphology and thickness of membranes were analyzed using field-emission scanning electron microscopy (FESEM) under a SU8010 microscope (Hitachi High-Technologies, Japan). Humidity-dependent surface morphology of the CM was analyzed using ESEM (XL-30 FEG, FEI, USA). The hydrophilicity of the samples was investigated by measuring the contact angle using a model DSA100 analyzer (KRUSS GmbH, Germany). The electrical properties were characterized using a B2901A source measurement unit (Keysight Technologies, USA).

Self-healing gate–based releasing mechanism

To quickly form a conductive path between the skin and the surface of the sensor when the CM is attached to the skin with dense hair layer (fig. S4, E and G), a self-healing gate–based releasing mechanism was developed. The perforated pore inside the CM is reopened by a contact pressure of 9.8 to 17.6 kPa generated when attaching the CS to the skin. At that time, approximately 20 to 30 μl of saline solution is released to the skin (fig. S3E). The saline penetrates into the dense hair layers (fig. S4E) to form a conductive interface between the skin and CS. The gate then recloses by the self-healing effect of the CM. If an extra electrolyte is required to maintain the electrical sensor-skin interface for long-term measurement, a small amount of saline solution can be supplied through the pore reopened by electrode-finger pressure (fig. S3D).

Mechanics of finite-element analysis simulation of biosensors

COMSOL (ver. 5.4) commercial software was used to study the release mechanism of the biosensors. Two-dimensional finite-element analysis was used to calculate the flow density of the biosensor (fig. S3, D and E). To simplify the analysis, the sensor was modeled using two domains. Boundary conditions corresponding to pressure were applied on the top of the reservoir. The dynamic viscosity (v) and density (ρ) of saline solution are as follows: $v_{\text{saline solution}} = 1000$ Pa·s and $\rho_{\text{saline solution}} = 1.0$ kg/m^3.

In vitro biocompatible test

The cell viability and proliferation rate were analyzed using an indirect method. Human keratinocyte cells were grown in an incubator with a 5% CO_2 atmosphere at 37°C. The samples were cleaned with ethanol and ultraviolet exposure. The samples were then placed in 24-well plates, and 1 ml of the solution containing the fibroblast cells was seeded on the samples. The cell density of the solution was 1×10^5 cells·ml^{-1}. The cell viability was analyzed using the Cell Counting Kit-8 (CCK-8). The light absorbance was measured at 450 nm using a VersaMax microplate reader (Molecular Devices LLC, USA). Before measuring the absorbance, 50 μl of the CCK-8 kit solution was dropped onto each sample and kept in the incubator for 2 hours. Next, 100-μl aliquots of the L929 cell suspension were seeded in the wells of a 96-well culture plate.

In vivo biocompatible test

To evaluate the biological responses of the subcutaneous tissues to the implanted material, we followed the International Organization for Standardization (ISO)–10993 and notification no. 2014-115 of Korea Ministry of Food and Drug Safety. Following ISO 10993-2, healthy male 6-week-old BALB/c mice with a mean ± SD body weight of 21.3 ± 0.8 g were used. The mice were obtained at 5 weeks of age from Orient Bio Co. (Republic of Korea) and maintained under an artificial 12-hour light/dark cycle at a constant temperature of 22 ± 1°C and constant humidity of 55 ± 10%. The mice were kept in their cages for 1 week to acclimate to the laboratory conditions.

Each mouse was subcutaneously implanted with a piece of CM and poly(dimethylsiloxane) (PDMS; Sylgard s18, Dow Corning, USA; 10:1 weight ratio of prepolymer to cross-linker) as a control following ISO 10993-6. Briefly, the mice were anesthetized with 2% isoflurane and the dorsal hair was removed by shaving. A sagittal skin incision was made on the back, and subcutaneous pouches were made. The CM and PDMS were prepared following ISO 10993-12 and finely cut into 10-mm-diameter circles. The samples were subcutaneously implanted at least 1 cm apart. The skin was sutured with nonabsorbable 6-0 silk. The mice were allowed unrestricted cage activity. Two weeks after surgery, the mice were euthanized in a CO_2 chamber and whole skins were freshly sampled for analysis.

To evaluate the local histopathological effects, freshly excised skin samples were fixed with 4% paraformaldehyde for 24 hours. The tissues were processed using routine tissue techniques and embedded in paraffin. The paraffin-embedded specimens were sliced into 4-μm-thick sections. The sections were then transferred to microscope slides. Subsequently, deparaffinized skin sections were stained with H&E. All stained sections were examined under a light microscope to assess histological changes generally indicative of irritation, including polymorphonuclear cell infiltration, mononuclear cell infiltration, necrosis, angiogenesis, fibrosis, and fatty infiltration. All operating procedures for handling of experimental animals were performed in accordance with guidelines and regulations of the Institutional Animal Care and Use Committee (IACUC) of Konkuk University, which was accredited for laboratory animal care by the Korea Ministry of Food and Drug Safety.

Skin erythema test

Skin compatibility tests were performed on one individual using the swollen CM. The biosensor surface was attached on the forearm for 4 days with a clinical usable air permeable tape (Himom Band, JW Pharmaceutical Corporation). The skin reaction (itching and erythema) was investigated (fig. S1H). This test was approved by the Institutional Review Board of Korea University, Seoul, Republic of Korea (IRB no. 1040548-KU-IRB-18-101-A-2).

Measurement of electrical resistance, conductivity, and electromechanical stability of the CM

The circular CMs with 3-cm diameter and 20-μm thickness were sandwiched with top and bottom electrodes. A PDMS (Sylgard 184 kit) film was cut with an opening (4 cm^2), which served as a well for holding the electrolyte solution. Electrolytes were filled into a molded PDMS well. The electrical resistance was recorded from a CM using a pair of top and bottom electrodes using a multimeter (Keysight 34460A) interfaced with computerized recording software (BenchVue 3.7).

For electrochemical stability tests of the swollen CM, we varied the RH through a homemade humidifier. Briefly, air bubbling through a water-containing conical flask was led into a gas-purge desiccator cabinet, and the gas flow rate was adjusted to control the RH in the desiccator cabinet. The RH and temperature were monitored in real time using a thermohygrometer (P330, Swiss). We used the bubbler method to control the RH in high-humidity environments. Variations of resistance were measured using a two-probe method. Electromechanical stability of the samples as a function of the number of bending cycles was measured by repeated bending using a homemade bending system. A 2.0-cm-long CM underwent release bending for up to 10,000 cycles with simultaneous recording of electrical resistance.

Measurement setup of EP signals

The impedance and EP signals were measured using a BrainAmp DC system (Brain Products GmbH, Germany). The impedance value of each channel at 10 Hz was recorded automatically using a BrainVision system (Brain Products GmbH, Germany). The instrument only measures values between 0 and 100 kilohms. The sampling rate was 1000 Hz, and the band-pass filter was set at 0.3 to 70 Hz. A notch filter was applied at 50 Hz. The EIS test under a frequency range of 0.1 to 1000 Hz was conducted in an electrochemical workstation (CHI750E, CH Instruments Inc., USA) using a two-electrode system. The distance between the two-electrode centers on the scalp was 4 cm. The current was applied on the electrode pair to measure the contact impedance. The amplitude of the test signal for the impedance test was 5 mV, and the frequency of the test signal ranged from 0.1 to 1000 Hz. A commercial 64-channel EEG cap (EASYCAP GmbH, Germany) was used to mount the electrodes. The results of the average EIS were derived through six trials.

Multiple experimental procedures

To quantitatively verify the performance of the CS, various experiments were conducted. These experiments were approved by the Institutional Review Board of Korea University, Seoul, Republic of Korea (IRB no. 1040548-KU-IRB-18-101-A-2). The experiments addressed electrochemical stability, verification on various skins (including people from Asian and Western countries), long-term stability, stability concerning severe detachment artifacts, simultaneous monitoring of multiple EP signals, stability in dynamic environments, and offline-online BCI application. A total of 60 individuals aged 20 to 40 years participated in the experiments (table S1). A numerical program (MATLAB, MathWorks, USA) was used to preprocess, separate, and classify datasets. For signal processing, BBCI-Toolbox (*46*), EEGLAB (*53*), and OpenBMI toolbox (*47*) were applied.

Electrochemical stability

An OCP experiment was conducted to examine the electrochemical stability of CS. An Ag/AgCl electrode was used as the reference electrode. Each OCP value of the Ag/AgCl and CS was measured in a saline solution for 10 min using a model 2100 multimeter (Keithley Instrument Inc., USA). Equilibrium electrode potential, defined as the average potential value within 10 min, was determined to evaluate electrode polarization characteristics.

In the test of OCP for the stability of polarization voltage, the potential of Ag/AgCl oscillated between −594.57 and 396.65 μV and that of CS oscillated between −793.36 and 409.88 μV (fig. S4, C and D). The average equilibrium potentials of Ag/AgCl and CS were −12.94 ± 61.41 and −31.27 ± 81.15 μV, respectively (fig. S4D).

Verification on various scalps

Participants included 10 Asians and 8 Westerners. Two of the Westerners were women with long hair. In experiments involving the Westerners, impedance and EEG were measured from five channels of CSs (FP1, FP2, Oz, O1, and O2) (fig. S4E). AFz and the right mastoids served as ground and reference electrodes, respectively. Eye open/closed/blink paradigm (eye opening for 10 s, eye closing for 10 s, followed by eye blinking for 10 s) was used. For Asians, impedance and EEG were measured from 10 channels (GSs: FP1, FP2, Oz, O1, and O2; CSs: AF7, AF8, POz, PO7, and PO8) (fig. S4G). The same eye open/closed and SSVEPs paradigms (5, 7.5, and 10 Hz) were used. To quantify the signal quality of the dataset related to

SSVEP between the CSs and GSs, Pearson's correlation coefficient analysis was conducted (fig. S5A). In addition, SNR analysis of SSVEPs for channels positioned to the visual cortex region was performed (GSs: Oz, O1, and O2; CSs: POz, PO7, and PO8). The energy of $y(f)$ was calculated using fast Fourier transform. For SSVEPs at a stimulation frequency f, the SNR in decibels was defined as the ratio of $y(f)$ to the mean value of the two adjacent frequencies as follows

$$\mathrm{SNR} = 20 \times \log_{10} \frac{y(f)}{(y(f-1)+y(f+1))}$$

For the SSVEP (5, 7.5, and 10 Hz) paradigm, the grand average SNR of CSs and GSs was 22.701 ± 10.96 and 23.835 ± 9.67, respectively (fig. S5B). There was no significant difference in the two-sample test ($P = 0.3659$). In the PSD analysis, the peaks corresponding to the stimulation frequencies were clearly detected (fig. S5C).

Long-term stability

For the long-term experiment, impedance measurements and EEG recordings were performed using the eye open/closed paradigm for 8 hours daily for 7 days. The electrode setup consisted of 11 GSs and 11 CSs. All positions of the electrodes were based on the international 10-20 system (GS: FP1, FP2, Cz, C3, C4, Pz, P3, P4, Oz, O1, and O2; CS: AF7, AF8, FCz, C5, C6, CPz, P5, P6, POz, PO7, and PO8). Seven individuals participated in this experiment. To evaluate the impedance stability, impedance variation was defined as the value of impedance over time minus the value of initial impedance. To quantify the signal quality of dataset related to alpha rhythm between the CSs and GSs, Pearson's correlation coefficient analysis was conducted (fig. S5D). In addition, for the SNR analysis (*10*) in the alpha rhythm, data between 8 and 12 Hz were applied. SNR was calculated as

$$\mathrm{SNR} = 20 \times \log_{10} \frac{\text{eye closed data}}{\text{eye open data}}$$

Recovery time after sensor detachment

A sensor detachment experiment was conducted to verify the effect of the scalp-sensor owing to the severe motion artifact generated by an external force. Detachment of the sensors was conducted at intervals of 6 s, determined using a metronome. The attachment process of the sensors was not performed separately. Sensor-scalp reattachment was reset automatically by the elasticity of the electrode cap. A total of 180 sensor detachments on the scalp of nine individuals were conducted, and the impedance was recorded for the detachment. The recovery time was calculated from the time that the sensor was reset to the time that the sensor began to remeasure the normal EEG. The criteria for normal EEG were set when the impedance was <100 kilohms and the amplitude of the signal oscillated between 0 and 100 μV.

Simultaneous monitoring of multiple biosignals

To decode the drowsy, awake, or movement state of the user, multiple EP signals were simultaneously measured. To record the EEG, ECG, and EMG signals simultaneously, AFz and right mastoid positions served as the ground and reference electrodes, respectively. The sensors recorded the signals on Cz and FCz channels for EEG, on the right forearm for EMG, and on the left forearm for ECG.

For the detection of movement intention, a handgrip was used as an application. The eight users grabbed the handgrip with their right hand and attempted a grip 20 times at an interval of 3 s produced by a metronome. For MRCP analysis, downsampling of 100 Hz and a filter of 0.1 to 1 Hz were applied (*42*). EEG and EMG data were also segmented from 0 to 3000 ms with respect to stimulus onset. Average MRCP and EMG were compared using time-amplitude analysis.

To monitor the drowsy state, nine individuals were instructed to close the eyes for approximately 15 min and allowed to drowse in a soft armrest chair. The laboratory light was turned off and the room was kept quiet. Nine individuals participated in this experiment.

In addition, experiments for single EMG and ECG measurements based on our previous study (*12*) are reported in fig. S6 (A to C). The average impedance of CSs across 14 individuals was 18.9 ± 9.2 kilohms on the wrist for ECG and 24.8 ± 9.5 kilohms on the arm for EMG.

Offline and online BCI

BCI experiments were conducted to quantify the performances of CSs. As the experimental paradigm, the binary MI and four-class SSVEP paradigms were applied. All experiment programs and analysis methods were based on our previous study (*47*). The analysis code and toolbox are available in the GitHub (https://github.com/PatternRecognition/OpenBMI) and BCI (http://openbmi.org) websites. The EEG channels were set to each of the 16 GS and 16 CS channels (fig. S6G), and 17 individuals participated.

BCI in a dynamic environment

To verify the sensing ability of CSs in a dynamic environment, an experiment was conducted in which individuals performed BCI paradigms while cycling on an exercise bicycle (Iwha Sean Lee X Bike Inc., Republic of Korea). The BCI paradigm (the four-class SSVEP paradigm) involved a rest state, a cycling 1 set (20 min), and a cycling 2 set (20 min). To analyze the variation of performances of CSs as influenced by sweat, the eye open/closed paradigms were conducted in the rest state, immediately after the cycling 1 set, and immediately after the cycling 2 set.

Eight BCI naïve individuals participated in the experiment: Participants cycled, on average, 6.0 ± 1.0 km at an average speed of 9.2 ± 1.9 km/h for 40 min, and they burned approximately 193.75 ± 33.47 cal. EEG signals were measured from the CSs of six channels (FP1, FP2, Cz, Oz, O1, and O2), and the performance of CSs was quantified through impedance measurement, alpha rhythm SNR, and SSVEP classification accuracy.

Deep learning-based real-time BCI game system

The experiment was conducted to apply the CSs to a real-time game control system. The game system used in this experiment is a software called Brain Runner that controls a virtual avatar (i.e., an obstacle race game using BCI; BCI racing) (*6*). The experiment was conducted with a 16-channel CSs setting. Eight BCI naïve individuals participated. The user performed four classes of MI (right hand, left hand, foot, and resting state) to collect datasets of a total of 30 trials corresponding to each class. Conventional augmented common spatial patterns and convolution neural network (CNN) architectures (*52*) were applied for feature extraction and classifier parameter learning of the MI datasets. Two CNN architectures learned the datasets using two convolutional layers and one fully connected layer before the output layer. The input data to the network were an array

of frequency bands, pattern size, and the number of the epoch. The first CNN training involved 32 feature maps (size: 32 × 1) in the first convolution layer. Next, the convolution layer also involved 32 feature maps (size: 1 × 20). The number of units in the fully connected layer was 480, and the training involved feeding a training batch of 20 and epochs of approximately 20. The second CNN training involved 48 feature maps (size: 1 × 96) in the first convolution layer. Next, the convolution layer also involved 48 feature maps (size: 1 × 80). The number of units in the fully connected layer was 1280 and involved feeding a training batch of 5 and epochs of approximately 50. In the testing phase, we applied the first CNN model to classify the brain patterns of MI and the resting state. Then, the other CNN model was applied to classify the patterns of three-class MI. In the classifier training phase, the classification accuracy for multiclass MI (right hand, left hand, foot, and rest) averaged 51.4 ± 6.6% through fivefold cross-validation. For real-time operation, features were calculated every 40 ms with a 3-s sliding window. The categorized patterns were converted into commands, and the game avatar was controlled via user datagram protocol communication.

SUPPLEMENTARY MATERIALS

Supplementary material for this article is available at http://advances.sciencemag.org/cgi/content/full/7/16/eabe7432/DC1

REFERENCES AND NOTES

1. T. Someya, M. Amagai, Toward a new generation of smart skins. *Nat. Biotech.* **37**, 382–388 (2019).
2. Y. Chen, Y. Zhang, Z. Liang, Y. Cao, Z. Han, X. Feng, Flexible inorganic bioelectronics. *npj Flex. Electron.* **4**, 2 (2020).
3. M. A. L. Nicolelis, M. A. Lebedev, Principles of neural ensemble physiology underlying the operation of brain–machine interfaces. *Nat. Rev. Neurosci.* **10**, 530–540 (2009).
4. J. d. R. Millán, R. Rupp, G. R. Müller-Putz, R. Murray-Smith, C. Giugliemma, M. Tangermann, C. Vidaurre, F. Cincotti, A. Kübler, R. Leeb, C. Neuper, K.-R. Müller, D. Mattia, Combining brain-computer interfaces and assistive technologies: State-of-the-art and challenges. *Front. Neur.* **4**, 161 (2010).
5. K.-R. Müller, M. Tangermann, G. Dornhege, M. Krauledat, G. Curio, B. Blankertz, Machine learning for real-time single-trial EEG-analysis: From brain–computer interfacing to mental state monitoring. *J. Neur. Meth.* **167**, 82–90 (2008).
6. D. Novak, R. Sigrist, N. J. Gerig, D. Wyss, R. Bauer, U. Götz, R. Riener, Benchmarking brain-computer interfaces outside the laboratory: The Cybathlon 2016. *Front. Neurosci.* **11**, 756 (2018).
7. L.-D. Liao, C.-T. Lin, K. McDowell, A. E. Wickenden, K. Gramann, T.-P. Jung, L.-W. Ko, J.-Y. Chang, Biosensor technologies for augmented brain–computer interfaces in the next decades. *Proc. IEEE* **100**, 1553–1566 (2012).
8. P. Pedrosa, P. Fiedler, L. Schinaia, B. Vasconcelos, A. C. Martins, M. H. Amaral, S. Comani, J. Haueisen, C. Fonseca, Alginate-based hydrogels as an alternative to electrolytic gels for rapid EEG monitoring and easy cleaning procedures. *Sens. Actuators B* **247**, 273–283 (2017).
9. P. Fiedler, R. Muhle, S. Griebel, P. Pedrosa, C. Fonseca, F. Vaz, F. Zanow, J. Haueisen, Contact pressure and flexibility of multipin dry EEG electrodes. *IEEE Trans. Neural Syst. Rehabil. Eng.* **26**, 750–757 (2018).
10. G. Li, D. Zhang, S. Wang, Y. Y. Duan, Novel passive ceramic based semi-dry electrodes for recording electroencephalography signals from the hairy scalp. *Sens. Actuators B* **237**, 167–178 (2016).
11. D.-H. Kim, N. Lu, R. Ma, Y.-S. Kim, R.-H. Kim, S. Wang, J. Wu, S. M. Won, H. Tao, A. Islam, K. J. Yu, T.-i. Kim, R. Chowdhury, M. Ying, L. Xu, M. Li, H.-J. Chung, H. Keum, M. M. Cormick, P. Liu, Y.-W. Zhang, F. G. Omenetto, Y. Huang, T. Coleman, J. A. Rogers, Epidermal electronics. *Science* **333**, 838–843 (2011).
12. Y. J. Yun, J. Ju, J. H. Lee, S.-H. Moon, S.-J. Park, Y. H. Kim, W. G. Hong, D. H. Ha, H. Jang, G. H. Lee, H.-M. Chung, J. Choi, S. W. Nam, S.-H. Lee, Y. Jun, Highly elastic graphene-based electronics toward electronic skin. *Adv. Funct. Mater.* **27**, 1701513 (2017).
13. B. Katherine, Moving skin beyond the biological. *Nature* **563**, S96–S98 (2018).
14. C. Blanpain, E. Fuchs, Epidermal homeostasis: A balancing act of stem cells in the skin. *Nat. Rev. Molec. Cell Bio.* **10**, 207–217 (2009).
15. L. Gravitz, Skin. *Nature* **563**, S83 (2018).
16. J. Gould, Superpowered skin. *Nature* **563**, S84–S85 (2018).
17. T. H. Yeats, J. K. C. Rose, The formation and function of plant cuticles. *Plant Physiol.* **163**, 5–20 (2013).
18. A. Daszkowska-Golec, I. Szarejko, Open or close the gate—Stomata action under the control of phytohormones in drought stress conditions. *Front. Plant Sci.* **4**, 138 (2013).
19. G. Miller, N. Suzuki, S. Ciftci-Yilmaz, R. Mittler, Reactive oxygen species homeostasis and signalling during drought and salinity stresses. *Plant Cell Environ.* **33**, 453–467 (2010).
20. J.-K. Zhu, Abiotic stress signaling and responses in plants. *Cell* **167**, 313–324 (2016).
21. J. Negi, O. Matsuda, T. Nagasawa, Y. Oba, H. Takahashi, M. Kawai-Yamada, H. Uchimiya, M. Hashimoto, K. Iba, CO_2 regulator SLAC1 and its homologues are essential for anion homeostasis in plant cells. *Nature* **452**, 483–486 (2008).
22. X. He, M. Aizenberg, O. Kuksenok, L. D. Zarzar, A. Shastri, A. C. Balazs, J. Aizenberg, Synthetic homeostatic materials with chemo-mechano-chemical self-regulation. *Nature* **487**, 214–218 (2012).
23. M. M. Lerch, A. Grinthal, J. Aizenberg, Viewpoint: Homeostasis as inspiration—Toward interactive materials. *Adv. Mater.* **32**, 190554 (2020).
24. D. Klemm, B. Heublein, H.-P. Fink, A. Bohn, Cellulose: Fascinating biopolymer and sustainable raw material. *Angew. Chem. Int. Ed.* **44**, 3358–3393 (2005).
25. B. Thomas, M. C. Raj, A. K. B, R. M. H, J. Joy, A. Moores, G. L. Drisko, C. Sanchez, Nanocellulose, a versatile green platform: From biosources to materials and their applications. *Chem. Rev.* **118**, 11575–11625 (2018).
26. S. Rongpipi, D. Ye, E. D. Gomez, E. W. Gomez, Progress and opportunities in the characterization of cellulose—An important regulator of cell wall growth and mechanics. *Front. Plant Sci.* **9**, 1894 (2019).
27. N. Aarne, E. Kontturi, J. Laine, Influence of adsorbed polyelectrolytes on pore size distribution of a water-swollen biomaterial. *Soft Matter* **8**, 4740–4749 (2012).
28. Z. Jahan, M. B. K. Niazi, Ø. W. Gregersen, Mechanical, thermal and swelling properties of cellulose nanocrystals/PVA nanocomposites membranes. *J. Ind. Eng. Chem.* **57**, 113–124 (2018).
29. S. Wang, A. Lu, L. Zhang, Recent advances in regenerated cellulose materials. *Prog. Polym. Sci.* **53**, 169–206 (2016).
30. G. Jiang, W. Huang, L. Li, X. Wang, F. Pang, Y. Zhang, H. Wang, Structure and properties of regenerated cellulose fibers from different technology processes. *Carboh. Polym.* **87**, 2013–2018 (2012).
31. L. R. Hochberg, D. Bacher, B. Jarosiewicz, N. Y. Masse, J. D. Simeral, J. Vogel, S. Haddadin, J. Liu, S. S. Cash, P. van der Smagt, J. P. Donoghue, Reach and grasp by people with tetraplegia using a neurally controlled robotic arm. *Nature* **485**, 372–375 (2012).
32. M. Mahmood, D. Mzurikwao, Y.-S. Kim, Y. Lee, S. Mishra, R. Herbert, A. Duarte, C. S. Ang, W.-H. Yeo, Fully portable and wireless universal brain–machine interfaces enabled by flexible scalp electronics and deep learning algorithm. *Nat. Mach. Intell.* **1**, 412–422 (2019).
33. L. M. Jenkins, A. M. Donald, Use of the environmental scanning electron microscope for the observation of the swelling behaviour of cellulosic fibres. *Scanning* **19**, 92–97 (1997).
34. A. M. Donald, The use of environmental scanning electron microscopy for imaging wet and insulating materials. *Nat. Mater.* **2**, 511–516 (2003).
35. D. Le Bras, M. Strømme, A. Mihranyan, Characterization of dielectric properties of nanocellulose from wood and algae for electrical insulator applications. *J. Phys. Chem. B* **119**, 5911–5917 (2015).
36. H. Golmohammadi, E. Morales-Narváez, T. Naghdi, A. Merkoçi, Nanocellulose in sensing and biosensing. *Chem. Mater.* **29**, 5426–5446 (2017).
37. C. Yang, Z. Suo, Hydrogel ionotronics. *Nat. Rev. Mat.* **3**, 125–142 (2018).
38. G. Li, S. Wang, Y. Y. Duan, Towards gel-free electrodes: A systematic study of electrode-skin impedance. *Sens. Actuators B* **241**, 1244–1255 (2017).
39. A. Cömert, J. Hyttinen, Impedance spectroscopy of changes in skin-electrode impedance induced by motion. *Biomed. Eng. Online* **13**, 149 (2014).
40. T. J. Swick, The neurology of sleep: 2012. *Sleep Med. Clinics* **7**, 399–415 (2012).
41. E. C.-P. Chua, W.-Q. Tan, S.-C. Yeo, P. Lau, I. Lee, I. H. Mien, K. Puvanendran, J. J. Gooley, Heart rate variability can be used to estimate sleepiness-related decrements in psychomotor vigilance during total sleep deprivation. *Sleep* **35**, 325–334 (2012).
42. J. Pereira, A. I. Sburlea, G. R. Müller-Putz, EEG patterns of self-paced movement imaginations towards externally-cued and internally-selected targets. *Sci. Rep.* **8**, 13394 (2018).
43. B. Blankertz, R. Tomioka, S. Lemm, M. Kawanabe, K.-R. Müller, Optimizing spatial filters for robust EEG single-trial analysis. *IEEE Sign. Proc. Mag.* **25**, 41–56 (2008).
44. S. Lemm, B. Brankertz, T. Dickhaus, K.-R. Müller, Introduction to machine learning for brain imaging. *Neuroimage* **56**, 387–399 (2011).
45. B. Blankertz, S. Lemm, M. Treder, S. Haufe, K.-R. Müller, Single-trial analysis and classification of ERP components––A tutorial. *Neuroimage* **56**, 814–825 (2011).
46. B. Blankertz, L. Acqualagna, S. Dähne, S. Haufe, M. Schultze-Kraft, I. Sturm, M. Uščumlic, M. A. Wenzel, G. Curio, K.-R. Müller, The Berlin brain-computer interface: Progress beyond communication and control. *Front. Neur.* **10**, 530 (2016).

47. M.-H. Lee, O.-Y. Kwon, Y.-J. Kim, H.-K. Kim, Y.-E. Lee, J. Williamson, S. Fazli, S.-W. Lee, EEG dataset and OpenBMI toolbox for three BCI paradigms: An investigation into BCI illiteracy. *GigaScience* **8**, giz002 (2019).
48. A. von Lühmann, Z. Boukouvalas, K.-R. Müller, T. Adalı, A new blind source separation framework for signal analysis and artifact rejection in functional Near-Infrared Spectroscopy. *Neuroimage* **200**, 72–88 (2019).
49. R. Zink, B. Hunyadi, S. Van Huffel, M. De Vos, Mobile EEG on the bike: Disentangling attentional and physical contributions to auditory attention tasks. *J. Neur. Eng.* **13**, 046017 (2016).
50. L. Kalevo, T. Miettinen, A. Leino, S. Kainulainen, H. Korkalainen, K. Myllymaa, J. Toyras, T. Leppanen, T. Laitinen, S. Myllymaa, Effect of sweating on electrode-skin contact impedances and artifacts in EEG recordings with various screen-printed Ag/Agcl electrodes. *IEEE Access* **8**, 50934–50943 (2020).
51. G. Li, S. Wang, Y. Y. Duan, Towards conductive-gel-free electrodes: Understanding the wet electrode, semi-dry electrode and dry electrode-skin interface impedance using electrochemical impedance spectroscopy fitting. *Sens. Actuators B* **277**, 250–260 (2018).
52. H. Yang, S. Sakhavi, K. K. Ang, C. Guan, On the use of convolutional neural networks and augmented CSP features for multi-class motor imagery of EEG signals classification, in *Proceedings of the IEEE 29th Annual International Conference of Engineering in Medicine and Biology Society, EMBS 2015* (2015), pp. 2620–2623.
53. A. Delorme, S. Makeig, EEGLAB: An open source toolbox for analysis of single-trial EEG dynamics including independent component analysis. *J. Neurosci. Methods* **134**, 9–21 (2004).

Acknowledgments: We thank A. von Lühmann (Machine Learning Department, Technical University of Berlin) for providing technical support in the recording and analysis of EEG signals. **Funding:** This work is supported by the Institute for Information and Communications Technology Planning and Evaluation (IITP) grant funded by the Korea Government (MSIT) (Development of BCI-based Brain and Cognitive Computing Technology for Recognizing User's Intentions Using Deep Learning) under grant 2017-0-00451, (Development of Intelligent Pattern Recognition Softwares for Ambulatory Brain Computer Interface) under grant 2015-0-00185, and (Artificial Intelligence Graduate School Program, Korea University) under grant 2019-0-00079. **Author contributions:** J.-Y.K. conceived the ideas, developed the sensor, designed and performed electrochemical and BCI experiments, analyzed the signals using machine learning, and wrote the manuscript. Y.J.Y. addressed the idea of the sensor, comprehensively analyzed the materials, designed and performed chemical-mechanical-electrical experiments, and wrote the manuscript. J.J. provided the key ideas for sensor principle and structure. C.-Y.K. designed and performed in vivo and in vitro biosafety tests on the materials. K.-R.M. provided advice and supervision and wrote the manuscript. S.-W.L. conceived the project, supervised the project, and wrote the manuscript. **Competing interests:** The authors declare that they have no competing interests. **Data and materials availability:** All data needed to evaluate the conclusions in the paper are present in the paper and/or the Supplementary Materials. Additional data related to this paper may be requested from the authors. The analysis code and toolbox are available in the GitHub (https://github.com/PatternRecognition/OpenBMI) and BCI (http://openbmi.org) websites. Requests for BCI racing system and raw data should be addressed to S.-W.L.

Submitted 11 September 2020
Accepted 26 February 2021
Published 16 April 2021
10.1126/sciadv.abe7432

Citation: J.-Y. Kim, Y. J. Yun, J. Jeong, C.-Y. Kim, K.-R. Müller, S.-W. Lee, Leaf-inspired homeostatic cellulose biosensors. *Sci. Adv.* **7**, eabe7432 (2021).